

A Novel Stealthy Target Detection Based on Stratospheric Balloon-borne Positional Instability due to Random Wind

Mohamed A. BARBARY¹, Peng ZONG²

¹ Dept. of Electronic and Information Engineering, Nanjing University of Aeronautics and Astronautics, Nanjing, China

² Dept. of Astronautics, Nanjing University of Aeronautics and Astronautics, Nanjing, China

mbarbary300@gmail.com, pengzong@nuaa.edu.cn

Abstract. A novel detection for stealthy target model F-117A with a higher aspect vision is introduced by using stratospheric balloon-borne bistatic system. The potential problem of the proposed scheme is platform instability impacted on the balloon by external wind force. The flight control system is studied in detail under typical random process, which is defined by Dryden turbulence spectrum. To accurately detect the stealthy target model, a real Radar Cross Section (RCS) based on physical optics (PO) formulation is applied. The sensitivity of the proposed scheme has been improved due to increasing PO-scattering field of stealthy model with higher aspect angle comparing to the conventional ground-based system. Simulations demonstrate that the proposed scheme gives much higher location accuracy and reduces location errors.

Keywords

Stealthy RCS, bistatic balloon-borne radar, PO method.

1. Introduction

The complexity of stealth target detection is not only related to the target itself, but also influenced by the electromagnetic environment [1]. The countering-stealth technologies are increasingly relevant, and research in this field is ongoing around the world. Stealth technology mostly focuses on defeating conventional ground-based detection radar. Thus, the success of counter stealth endeavors is focused mostly on novel and unique air defense infrastructure configurations. The Radar Cross Section (RCS) is an important evaluation criterion of aircraft's stealthy performance, the envelope of the backscatter from stealthy target varies rapidly with aspect angle. The shaping of stealthy objects to reduce the backscattered energy towards the radar is believed to be less effective when bistatic radar is used [2].

Several researches deal with improving stealthy target detection and tracking based on ground-based bistatic or netted radar system [2–8]. These researches didn't evaluate bistatic radar sensitivity and performance of stealthy

target with a higher aspect vision. Since the bistatic radar system might be mounted on higher altitude platforms to achieve a larger probability of detecting stealthy target, the bistatic radar sensitivity will be improved due to increasing the scattered field of stealthy target with higher altitude. In this paper, we investigate a novel technique for stealthy target detection based on balloon-borne bistatic radar system. The stations are positioned in the stratosphere about 21 km above the Earth and kept stable in a sphere of radius of 0.5 km [9]. To achieve high location accuracy for stealthy target, the proposed scheme uses a physical optics method (PO) to predict the real RCS of stealthy target. This will better represent the actual situation of the stealthy target detection.

One of the open research issues is whether the platforms positional instability due to sudden gusts of stratospheric winds. In the aerospace field, the study of turbulence effects is of fundamental importance in a lot of different aspects [10], such as improvements of the aerodynamic and structural analysis, prediction of expected behavior of a balloon-borne platform under various levels of turbulence, evaluation of the stability of onboard sensing equipment, and so on. Subject to the extreme complexity of the turbulence phenomena and due to the huge variety of applications, there is not a unique full-comprehensive model for the atmospheric turbulence, but there exist a wide variety of different and simplified models [11–12]. Numerous turbulence models are enumerated and described. The most commonly adopted model to study the impact of the turbulent wind gust on the balloon-borne is the Dryden model. According to this model, the atmospheric turbulence is modeled as a random velocity process added by balloon-borne velocity vector described in a body-fixed Cartesian coordinate system.

The rest of this paper is organized as follows. In Section 2, we present balloon positional instability analysis and random wind mathematical model. In Section 3, we discuss the PO formulation to predict RCS of stealth model. The bistatic range-measurement accuracy adopted for unstable position of the proposed scheme using stealth RCS is discussed in Section 4. Performance of the proposed scheme is evaluated via computer simulation in Section 5, followed by the conclusion in Section 6.

2. Balloon Positional Instability Analysis

The general dynamic equations of a stratospheric balloon platform are derived for flight over flat and non-rotating Earth, considering buoyancy, added mass and relevant conceptual design data of the stratospheric platform. To include the effect of jet stream as a moving wind field, the dynamic equations of motion can be derived in the relative wind-axes, inertial wind-axes, or body-axes coordinate systems [13–14]. The relative wind-axes system is more convenient than other coordinate systems because it expresses the wind-effect terms explicitly, bringing easier understanding. Fig. 1 illustrates the relationship between horizontal wind vector, airspeed velocity vector, and local (Earth-fixed) velocity of the platform. The wind-relative velocity vector is defined by airspeed V , flight path angle γ , and heading ψ .

From Fig. 1, the inertial flight velocity with respect to the local ENU frame is determined as:

$$\begin{aligned} V_I &= \dot{x}_i u + \dot{y}_i e + \dot{z}_i n \\ &= V + W \\ &= V \sin \gamma u + (V \cos \gamma \sin \psi + W_E)e + (V \cos \gamma \cos \psi + W_N)n \\ &= V_I \sin \gamma_I u + V_I \cos \gamma_I \sin \psi_I e + V_I \cos \gamma_I \cos \psi_I n. \end{aligned} \quad (1)$$

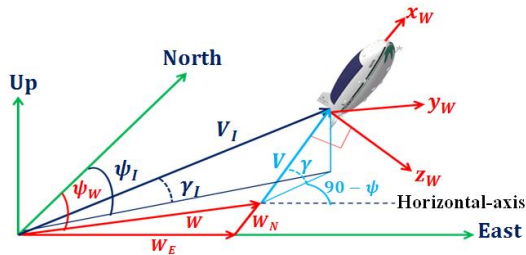


Fig. 1. Balloon-borne velocity in the local and wind-relative frames.

2.1 The Random Wind Mathematical Model

The Dryden model is one of the most useful and tractable models for atmospheric turbulence [13]. To define it we need a body-fixed reference frame attached to the gravity center of balloon-borne which moves with the target. The x-axis is on the position of motion direction, y-axis is on position along the wings, and z-axis is perpendicular to the balloon-borne plane. Then, the turbulence is modeled by adding some random components to balloon-borne velocity defined in the body-fixed coordinate system. An important consideration in this paper is the effect of steady-state horizontal winds. The horizontal wind velocity vector is defined as:

$$W_H = W \sin \psi_w e + W \cos \psi_w n, \quad (2)$$

$$= W_E e + W_N n. \quad (3)$$

In Dryden model continuous-time random processes are modeled as zero-mean, Gaussian-distributed processes whose PSD have analytic form given by [10–12]:

$$S_e(\omega) = \sigma_e^2 \frac{L_e}{\pi V_0} \frac{1}{1 + \left(\frac{L_e}{V_0} \omega\right)^2}, \quad (4)$$

$$S_n(\omega) = \sigma_n^2 \frac{L_n}{2\pi V_0} \frac{1 + 3\left(\frac{L_n}{V_0} \omega\right)^2}{\left[1 + \left(\frac{L_n}{V_0} \omega\right)^2\right]^2} \quad (5)$$

where V_0 is the gust wind speed in the balloon-borne system. The parameters σ_e^2 and σ_n^2 depend on the level of turbulence to be simulated and are selected accordingly [11]. Parameters L_e and L_n are the scale lengths for the PSDs and depend on the flight altitude. The mean wind velocity at the altitude of 21 km varies between -15 to +15 m/s [9]. Fig. 2 shows the PSDs of (4) and (5) for $\sigma_e = \sigma_n = \sigma_w = 15$ m/s, $L_e = L_n = 533.54$ m, and $V_0 = 15$ m/s. To reflect higher level of turbulence, the curves would be multiplied by the desired values of σ_e^2 and σ_n^2 .

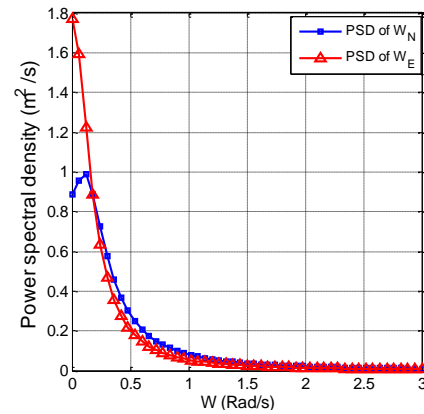


Fig. 2. PSD of Dryden velocity processes.

From (4) and (5), simulation model of wind can be written as:

$$\dot{W}_E + \frac{V_0}{L_e} W_E = \sqrt{\frac{2V_0}{L_e}} \xi_e, \quad (6a)$$

$$\dot{W}_1 + \frac{V_0}{L_n} W_1 = (\sqrt{3} - 1) \sqrt{\frac{V_0}{L_n}} \xi_n, \quad (6b)$$

$$\dot{W}_N + \frac{V_0}{L_n} W_1 + \frac{V_0}{L_n} W_N = \sqrt{\frac{3V_0}{L_n}} \xi_n \quad (6c)$$

where W_1 is the transition variable for calculating the wind field model, ξ_e and ξ_n are the random variables subject to normal distribution $N(0, \sigma_w^2)$.

2.2 External Forces Acting on Balloon Platform

The external forces acting on balloon-borne platform include aerodynamic lift L and drag D , thrust T , weight W and buoyancy B . We also consider a generic lateral force N , which may be generated by any means, such as rolling the lift vector through a small angle, ϕ , or applying lateral thrust. A free-body diagram of the forces in x-z plane is shown in Fig. 3.

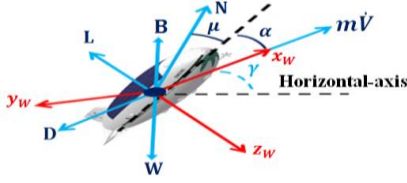


Fig. 3. External forces acting on balloon-borne platform.

The equations of motion are described by equating the time derivative of the momentum vector with the sum of external forces.

$$\begin{aligned} \sum F &= \frac{d}{dt}(M V_I) \\ &= [(B - W) \sin \gamma + T \cos(\alpha + \mu) - D] \hat{x} \\ &\quad + N \hat{y} + [(W - B) \cos \gamma - L - T \sin(\alpha + \mu)] \hat{z} \end{aligned} \quad (7)$$

where L and D are the lift and drag forces, respectively. The lift and drag coefficients from Lee [15] are used, and are assumed to vary only with angle of attack. μ represents the tilting angle of the propellers installed on both sides of the airship. The lift and drag force can be calculated by

$$L = q \cdot VOL^{2/3} \cdot C_L(\alpha), \quad D = q \cdot VOL^{2/3} \cdot C_D(\alpha), \quad (8a)$$

$$C_L(\alpha) = 0.590\alpha^4 + 1.2231\alpha^3 + 0.3248\alpha^2 + 0.921\alpha + 0.0118,$$

$$C_D(\alpha) = 0.340\alpha^4 + 0.0662\alpha^3 + 1.2248\alpha^2 + 0.0334\alpha + 0.04 \quad (8b)$$

where q and VOL represent the dynamic pressure of free stream and envelope volume of the platform.

The required thrust and power are given by [15]

$$T = q \cdot VOL^{2/3} \cdot C_D, \quad P = T \cdot V \cdot \frac{1}{\eta_p \eta_m} \quad (9)$$

where η_p and η_m represent the efficiency of the propellers and electric motor equipped in the airship. The values 0.7 and 0.9 are used for the efficiencies, respectively

The buoyancy force is another typical discriminator between LTA vehicles and conventional aircraft. It plays the role of lifting balloons upward and is equal to the weight of displaced air by its volume immersed in the atmosphere. The net lift that can be available for payload, system, and structure is determined by subtracting the weight of the lift gas and envelope [15]:

$$\begin{aligned} L_{net} &= B - W = VOL(\rho_a - \rho_h)g - W_{env}, \\ B &= VOL \cdot \rho_a \cdot g \end{aligned} \quad (10)$$

where ρ_a and ρ_h refer to the density of the surrounding atmosphere and helium, respectively. For the helium that is generally used as the lifting gas, the gross lift per unit volume $(\rho_a - \rho_h)g$ is 10.359 N/m^3 .

By Newton's second law, the force equilibrium equation in the inertial frame is expressed as

$$\begin{aligned} F &= m_T a = m_T \left(\frac{dV_I}{dt} \right)_I, \\ m_T &= m + m_{ax} + m_{ay} + m_{az} \end{aligned} \quad (11)$$

where m_T includes the empty mass m and the added masses, m_{ax} , m_{ay} , and m_{az} . When a body moves through fluid, it must push some mass of fluid out on the way. If the body is accelerated, the surrounding fluid must also be accelerated. Under this circumstance, the body behaves as if it were heavier, so that mass is added. The diagonal terms of added mass tensor are the main terms on the body axes of balloon for m_{ax} , m_{ay} , and m_{az} of (11) respectively. Because it is assumed that air density varies in a unit at operating altitude, the values should be multiplied by corresponding density to obtain added mass in the optimization process:

$$M_a = \begin{bmatrix} 2.1391 \times 10^4 & 1.6502 \times 10^{-12} & 1.3365 \times 10^{-11} \\ -2.0890 \times 10^{-12} & 2.4363 \times 10^5 & 9.8516 \times 10^1 \\ -2.2134 \times 10^{-12} & -9.8516 \times 10^1 & 2.4363 \times 10^5 \end{bmatrix} (\text{m}^3) \quad (12)$$

The total inertial acceleration is acceleration of airship with respect to local ENU frame, plus acceleration of ENU frame in inertial space, plus Coriolis acceleration. Using notation $(d/dt)_A$ to denote a derivative taken with respect to frame A, the inertial acceleration expressed in the wind frame is:

$$\begin{aligned} \left. \frac{dV_I}{dt} \right|_I &= \left. \frac{dV}{dt} \right|_I + \left. \frac{dW_I}{dt} \right|_I \\ &= \left. \frac{dV}{dt} \right|_w + \omega_w \times V|_w + C_l^w \times \left. \frac{dW_I}{dt} \right|_I \end{aligned} \quad (13)$$

where ω_w is angular rate of wind-axes frame regarding to the Earth-fixed frame and it satisfies

$$\omega_w = \begin{bmatrix} 1 & 0 & -\sin \gamma \\ 0 & \cos \phi & \sin \phi \cos \gamma \\ 0 & -\sin \phi & \cos \phi \cos \gamma \end{bmatrix} \begin{bmatrix} \dot{\phi} \\ \dot{\gamma} \\ \dot{\psi} \end{bmatrix}, \quad (14a)$$

$$C_l^w \times \left. \frac{dW_I}{dt} \right|_I = C_l^w \begin{bmatrix} \dot{W}_N \\ \dot{W}_E \\ 0 \end{bmatrix} = \begin{bmatrix} \dot{W}_{wx} \\ \dot{W}_{wy} \\ \dot{W}_{wz} \end{bmatrix}, \quad (14b)$$

and

$$C_l^w = \begin{bmatrix} C \gamma C \psi & C \gamma S \psi & -S \gamma \\ S \phi S \gamma C \psi - C \phi S \psi & S \phi S \gamma S \psi + C \phi C \psi & S \phi S \gamma \\ C \phi S \gamma C \psi + S \phi S \psi & C \phi S \gamma S \psi - S \phi C \psi & C \phi C \gamma \end{bmatrix} \quad (14c)$$

where C_l^w is the transformation matrix which transforms both of the local-level and wind-axes frames to each other, {C, S} mean cos and sin respectively. Combining equations (13) and (14) with (7) leads to the final representation of (11) in the wind-axes frame, after several algebraic manipulations. Finally, solving the simultaneous algebraic equations for the derivatives \dot{V} , $\dot{\gamma}$, and $\dot{\psi}$, the force equilibrium equations can be represented as

$$\dot{V} = \frac{(T \cos \alpha - D) - (mg - B) \sin \gamma}{m_T} - \dot{w}_{wx}, \quad (15a)$$

$$\begin{aligned} \dot{\gamma} &= \frac{(T \sin \alpha + L) \cos \phi - (mg - B) \cos \gamma}{m_T V} + \\ &\quad \frac{\dot{w}_{wz} \cos \phi + \dot{w}_{wy} \sin \phi}{V}, \end{aligned} \quad (15b)$$

$$\dot{\psi} = \frac{(T \sin \alpha + L) \sin \phi}{m_T V \cos \gamma} + \frac{\dot{w}_{wz} \sin \phi - \dot{w}_{wy} \cos \phi}{V \cos \gamma} \quad (15c)$$

where

$$\dot{w}_{wx} = \dot{w}_N \cos \gamma \cos \psi + \dot{w}_E \cos \gamma \sin \psi, \quad (16a)$$

$$\dot{w}_{wy} = \dot{w}_N (\sin \phi \sin \gamma \cos \psi - \cos \phi \sin \psi) + \dot{w}_E (\sin \phi \sin \gamma \sin \psi + \cos \phi \cos \psi), \quad (16b)$$

$$\dot{w}_{wz} = \dot{w}_N (\cos \phi \sin \gamma \cos \psi + \sin \phi \sin \psi) + \dot{w}_E (\cos \phi \sin \gamma \sin \psi - \sin \phi \sin \psi). \quad (16c)$$

3. The Physical Optics (PO) Formulation for Stealthy F-117A RCS Model

In the presence of a perfectly conducting surface, the total electromagnetic field of a source may be expressed as a superposition of the incident fields (E_i, H_i) and the fields (E_s, H_s) which are scattered by the surface. The scattered fields can be expressed in terms of the radiation integrals over actual currents induced on the surface of the scatterer. The PO assumes that the induced surface currents on the scatterer surface are given by the geometrical optics (GO) currents over those portions of the surface directly illuminated by the incident magnetic field, \vec{H}_i , and zero over the shadowed sections of the surface [16]:

$$\vec{J}_s = \begin{cases} 2\hat{n} \times \vec{H}_i & , \text{ illuminated region} \\ 0 & , \text{ shadow region} \end{cases} \quad (17)$$

where \hat{n} denotes the outward unit normal vector on a surface. The authors in this paper use PO method to predict RCS of a stealth target based on the geometry model of F-117A, which are modeled by the triangular facets. The geometry model of the stealth target based on F-117A is approximated by a model consisting of many triangular facets, in which there are a large number of points on the surface described in terms of Cartesian coordinates. This surface is then approximated by planar triangular facets connecting these points. An arbitrary midpoint p of the triangle surface is assigned coordinates (r_p, θ_p, ϕ_p) , the observation point is assigned coordinates (r_s, θ_s, ϕ_s) and unit vectors $(\hat{r}_s, \hat{\theta}_s, \hat{\phi}_s)$. Normal vector \hat{n} is a unit vector with its tip at the midpoint of triangle. Then \hat{n} can be expressed as cross product of vectors \vec{AB} and \vec{AC} . Once these vectors are found, \hat{n} can directly be found by $\hat{n} = \vec{AB} \times \vec{AC} / |\vec{AB}| |\vec{AC}|$. These parameters are depicted in Fig. 4.

Thus far, the discussion has involved the calculation of the scattered field from a single facet. Superposition is used to calculate the scattered field from the stealth target. First, the scattered field is computed for each facet. Then, the scattered field from each facet is vector summed to produce the total field in the observation direction. If the source is at a great distance from the target, it will illuminate the target with an incident field which is essentially a plane wave. The incident electric field intensity is given by $\vec{E}_i = (E_{i\theta} \hat{\theta}_i + E_{i\phi} \hat{\phi}_i) e^{-j\vec{k}_i \cdot \vec{r}_i}$, where $E_{i\theta}, E_{i\phi}$ are the

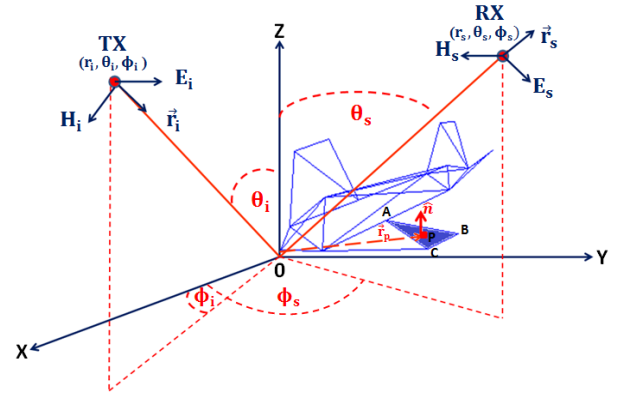


Fig. 4. Vector definitions of an approximation of a stealthy F-117A model using triangular facets on the surface.

orthogonal components in terms of the variables θ and ϕ , (r_i, θ_i, ϕ_i) are the spherical coordinates of the source and $(\hat{r}_i, \hat{\theta}_i, \hat{\phi}_i)$ are the unit vectors, so the magnetic field intensity of the incident field is given by:

$$\vec{H}_i = \frac{\vec{k}_i \times \vec{E}_i}{Z_0} = \frac{1}{Z_0} (E_{i\theta} \hat{\theta}_i - E_{i\phi} \hat{\phi}_i) e^{j\vec{k}_i \cdot \vec{r}_i} \quad (18)$$

where $(k = \frac{2\pi}{\lambda})$, \vec{k}_i is the propagation vector defined as $\vec{k}_i = -k(\hat{x} \sin \theta_i \cos \phi_i + \hat{y} \sin \theta_i \sin \phi_i + \hat{z} \cos \theta_i)$, Z_0 is the intrinsic impedance of free space and $h = \hat{r}_i \cdot \vec{r}_p = x_p \sin \theta_i \cos \phi_i + y_p \sin \theta_i \sin \phi_i + z_p \cos \theta_i$. Since radiation integral for the scattered field is calculated by employing a GO approximation for the currents induced on the surface, it can be concluded that PO is a high frequency method, which implies that target is assumed to be electrically large. For the scattered field, the vector potential is given by [17]:

$$\vec{A} = \frac{\mu}{4\pi r_s} e^{-jkr_s} \iint_s \vec{J}_s e^{j\vec{k}_s \cdot \vec{r}_p} ds \quad (19)$$

where μ is the permeability of a specific medium. For a far-field observation point, the following approximation holds

$$\begin{aligned} \vec{E}_s(r_s, \theta_s, \phi_s) &= -j\omega \vec{A} \\ &= -\frac{j\omega\mu}{2\pi r_s} e^{-jkr_s} \iint_s \hat{n} \times \vec{H}_i e^{j\vec{k}_s \cdot \vec{r}_p} ds \\ &= \frac{e^{-jkr_s}}{r_s} (E_{i\theta} \hat{\theta}_i - E_{i\phi} \hat{\phi}_i) \times \underbrace{\left(\frac{j}{\lambda} \right) \iint_s \hat{n} e^{j\vec{k}_s \cdot \vec{r}_p} ds}_{\vec{s}} \end{aligned} \quad (20)$$

where

$g = \hat{r}_s \cdot \vec{r}_p = x_p \sin \theta_s \cos \phi_s + y_p \sin \theta_s \sin \phi_s + z_p \cos \theta_s$. However, it is not possible to obtain an exact closed form solution for \vec{s} with this integral. Given that the incident wavefront is assumed plane and the incident field is known at the facet vertices, the amplitude and phase at the interior integration points can be found by interpolation. Then, the integrand can be expanded by using Taylor series, and each term integrated to give a closed form result. Usually, a small number of terms in Taylor series (on the order of 5) will give a sufficiently accurate approximation with unit amplitude plane wave ($|E_i| = 1$) [18].

$$\vec{S} = \left(\frac{j}{\lambda} \right) |\vec{AB} \times \vec{AC}| e^{jD_0} \left\{ \left[\frac{e^{jD_p}}{D_p(D_q - D_p)} \right] - \left[\frac{e^{jD_q}}{D_q(D_q - D_p)} \right] - \frac{1}{D_q D_p} \right\} \quad (21a)$$

where

$$D_p = k[(x_B - x_A) \sin \theta_s \cos \phi_s + (y_B - y_A) \sin \theta_s \sin \phi_s + (z_B - z_A) \cos \theta_s], \quad (21b)$$

$$D_q = k[(x_C - x_A) \sin \theta_s \cos \phi_s + (y_C - y_A) \sin \theta_s \sin \phi_s + (z_C - z_A) \cos \theta_s], \quad (21c)$$

$$D_0 = k[x_A \sin \theta_s \cos \phi_s + y_A \sin \theta_s \sin \phi_s + z_A \cos \theta_s]. \quad (21d)$$

It is now possible to write the formula of PO current as $\vec{J}_s = (J_{sx} \hat{x} + J_{sy} \hat{y} + J_{sz} \hat{z}) e^{jkh}$. In the general case, the local facet coordinate system will not be aligned with the global coordinate system. In the local facet coordinate system (x'', y'', z'') , the facet lies on the $x''y''$ plane, with \hat{z}'' being the normal to the facet surface, hence $\hat{n} = \hat{z}''$. For any arbitrary oriented facet with known global coordinates, its local coordinates can be obtained by a series of two rotations. First, angles α and β , are calculated by $\alpha = \arctan[n_y/n_x]$ and $\beta = \arccos(\hat{z} \cdot \hat{n})$, where $\hat{n} = n_x \hat{x} + n_y \hat{y} + n_z \hat{z}$. The local coordinates can be transformed to global coordinates [19]:

$$\begin{bmatrix} x'' \\ y'' \\ z'' \end{bmatrix} = \begin{bmatrix} \cos \beta & 0 & -\sin \beta \\ 0 & 1 & 0 \\ \sin \beta & 0 & \cos \beta \end{bmatrix} \begin{bmatrix} \cos \alpha & \sin \alpha & 0 \\ -\sin \alpha & \cos \alpha & 0 \\ 0 & 0 & 1 \end{bmatrix} \begin{bmatrix} x \\ y \\ z \end{bmatrix} \quad (22)$$

However, in facet local coordinates, the surface current does not have a \hat{z}'' component, since the facet lies on the $x''y''$ plane. Hence the local surface current is given by $\vec{J}_s = (J''_{sx} \hat{x}'' + J''_{sy} \hat{y}'') e^{jkh}$, the surface current components are [19]:

$$J''_{sx} = \left[\frac{E''_{i\theta} \cos \phi'' \cos \theta''}{2R_s + Z_0 \cos \theta''} - \frac{E''_{i\phi} \sin \phi''}{2R_s \cos \theta'' + Z_0} \right] \cos \theta'' \quad (23a)$$

$$J''_{sy} = \left[\frac{E''_{i\theta} \sin \phi'' \cos \theta''}{2R_s + Z_0 \cos \theta''} + \frac{E''_{i\phi} \cos \phi''}{2R_s \cos \theta'' + Z_0} \right] \cos \theta'' \quad (23b)$$

where $E''_{i\theta}, E''_{i\phi}$ are the components of the incident field in the local facet coordinates, θ'', ϕ'' are the spherical polar angles of the local coordinates and R_s being the surface resistivity of the facet material. When $R_s = 0$, the surface is a perfect electric conductor and assume that surface model is smoothing. To obtain the total scattered field, simply replace (23a) and (23b) in the radiation integral for the triangular facet, which was determined in (21a), the total number of facets ($m = 20$), so

$$\vec{E}_s(r_s, \theta_s, \phi_s) = \sum_{m=1}^{20} \frac{-jkZ_0 e^{-j(kr_s - D_{0m})}}{4\pi r_s} (J''_{s_m x} \hat{x}'' + J''_{s_m y} \hat{y}'') \times |\vec{AB}_m \times \vec{AC}_m| \times \left\{ \left[\frac{e^{jD_{Pm}}}{D_{Pm}(D_{Qm} - D_{Pm})} \right] - \left[\frac{e^{jD_{Qm}}}{D_{Qm}(D_{Qm} - D_{Pm})} \right] - \frac{1}{D_{Qm} D_{Pm}} \right\}. \quad (24)$$

Once the scattered field is known, RCS is computed in terms of the incident and scattered electric field intensities, and given by [20]:

$$RCS(r_s, \theta_s, \phi_s) = \lim_{R \rightarrow \infty} 4\pi R^2 \frac{|\vec{E}_s(r_s, \theta_s, \phi_s)|^2}{|\vec{E}_i|^2} \quad (25)$$

where R is the distance between the radar transmitter and target. For most objects, radar cross section is a three-dimensional map of the scattering contributions, which varies as a function of aspect angles (azimuth and elevation) and polarization. The scattering matrix describes the scattering behavior of a target as a function of polarization. Normally it contains four RCS values ($\theta\theta, \theta\phi, \phi\theta$ and $\phi\phi$), where the first letter denotes the transmission polarization, the second letter is the polarization at receive. Therefore, RCS can be derived at any polarizations:

$$RCS(r_s, \theta_s, \phi_s) = \lim_{R \rightarrow \infty} 4\pi R^2 \begin{bmatrix} |S_{\theta\theta}|^2 & |S_{\theta\phi}|^2 \\ |S_{\phi\theta}|^2 & |S_{\phi\phi}|^2 \end{bmatrix}. \quad (26)$$

The s_{pq} denotes the scattering parameter, whose first subscript specifies polarization of the receive antenna and the second one refers to polarization of the incident wave. The elements of scattering matrix are complex quantities and in terms of RCS [20]

$$RCS_{pq} = 4\pi R^2 S_{pq}^2 e^{-2j\psi_{pq}}, \quad \psi_{pq} = \arctan \left\{ \frac{\text{Im} \left(\frac{E_{sp}}{E_{iq}} \right)}{\text{Re} \left(\frac{E_{sp}}{E_{iq}} \right)} \right\}. \quad (27)$$

4. Range Accuracy under Positional Instability and Stealthy RCS Data

The bistatic geometry for a stealth target model considered in this paper is shown in Fig. 5, in which stealth target state $X = (p, V)^T = (x, y, z)^T$ is given in 3D Cartesian coordinates. In the same way the localizations of unstable balloon receiver and stationary transmitter are given respectively by $X_R = (P_R, V_R)^T = (x_R, y_R, z_R)^T$ and $X_T = (P_T, 0)^T = (x_T, y_T, z_T)^T$. Here we consider measurements in terms of bistatic range r , azimuth ϕ , elevation θ and bistatic range-rate \dot{r} , which is proportional to measured Doppler shift. The measurement equation without a root mean square measurement error (RMSE) $Z = (r, \phi, \theta, \dot{r})^T$ is given by:

$$r = \|P - P_T\| + \|P - P_R\|, \quad (28a)$$

$$\phi = \arctan \left[\frac{y - y_R}{x - x_R} \right], \quad (28b)$$

$$\theta = \arctan \left[\frac{z - z_R}{\sqrt{(x - x_R)^2 + (y - y_R)^2}} \right], \quad (28c)$$

$$\dot{r} = \left[\frac{(P - P_T) V}{\|P - P_T\|} \right] + \left[\frac{(P - P_R) (V - V_R)^T}{\|P - P_R\|} \right] \quad (28d)$$

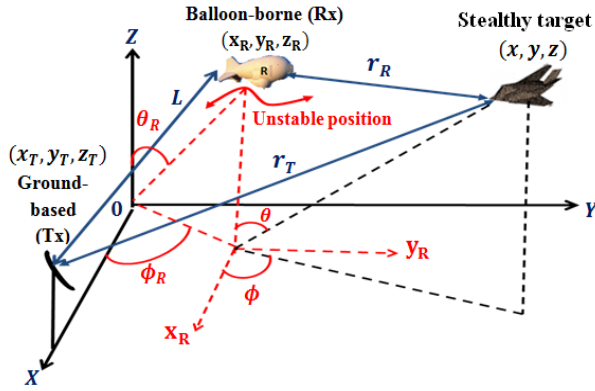


Fig. 5. The stealthy target detection under positional instability of balloon-borne bistatic radar system.

while the measurements at the receiver is characterized by root mean square measurement error (RMSE) as

$$\left. \begin{aligned} r^m &= r + \sigma_R \\ \phi^m &= \phi + \sigma_\phi \\ \theta^m &= \theta + \sigma_\theta \end{aligned} \right\} \quad (29)$$

The measurement accuracy is characterized by RMSE of σ_R , σ_ϕ , σ_θ computed by three error components [21].

$$\sigma_R = (\sigma_{RN}^2 + \sigma_{RF}^2 + \sigma_{RB}^2)^{1/2}, \quad (30a)$$

$$\sigma_\phi = (\sigma_{\phi N}^2 + \sigma_{\phi F}^2 + \sigma_{\phi B}^2)^{1/2}, \quad (30b)$$

$$\sigma_\theta = (\sigma_{\theta N}^2 + \sigma_{\theta F}^2 + \sigma_{\theta B}^2)^{1/2} \quad (30c)$$

where σ_{RN} , $\sigma_{\phi N}$, $\sigma_{\theta N}$ are SNR dependent random range and angular measurement errors, σ_{RF} , $\sigma_{\phi F}$, $\sigma_{\theta F}$ are range and angular fixed errors, and σ_{RB} , $\sigma_{\phi B}$, $\sigma_{\theta B}$ are range and angular bias errors. The SNR-dependent error usually dominates the radar range angular errors, which are random with a standard deviation and given by:

$$\sigma_{RN} = \frac{\Delta R}{\sqrt{2(SNR)}} = \frac{C}{2B\sqrt{2(SNR)}}, \quad (31a)$$

$$\sigma_{\phi N} = \sigma_{\theta N} = \frac{\theta_B / \cos(\phi \text{ or } \theta)}{K_M \sqrt{2(SNR)}} \quad (31b)$$

where B is the waveform bandwidth, C is the speed of light, ΔR is range resolution, θ_B is broadside beamwidth in the angular coordinate of the measurement, and K_M is mono-pulse pattern difference slope, assuming the value of broadside beamwidth is 1° and K_M is typically 1.6 [21]. The bistatic form of radar equation is developed here to evaluate bistatic radar sensitivity properties. The transmitter and the receiver are deployed at two separate locations, either or both of them changing with time. The receiver co-operates with transmitter through a synchronization link. Normally, a co-located Tx and Rx are not described as a bistatic system, even though they don't share a common antenna. Since the separation becomes significant relative to the typical target range, so that bistatic radar systems become relevant. It is also assumed that the target is an isotropic radiator, giving a constant RCS in all directions. Under these assumptions, it is reasonable to calculate bi-

static radar sensitivity by summing up the partial signal to noise ratio as [2]:

$$SNR = \frac{P_t G_t G_r RCS_B \lambda^2}{(4\pi)^3 K T_s B_n R_t^2 R_r^2 L} \quad (32)$$

where P_t is the peak transmitted power, G_t is the transmitter gain, G_r is the receiver gain, RCS_B is bistatic RCS of the target, λ is the transmitted wavelength, B_n is the bandwidth of the transmitted waveform, k is Boltzmann's constant, T_s is the receiving system noise temperature, L is the system loss for transmitter and receiver, R_t is the distance from the transmitter to the target and R_r is the distance from the target to the receiver. Most of the previous researches in bistatic radar sensitivity only considered the simplest case of bistatic radar sensitivity by isotropic radiator giving a constant RCS in all directions except for the distance from the transmitter and receiver to the target [3–8]. But this is not an accurate consideration to calculate the SNR of stealth target because the RCS value varies with elevation angle and azimuth angles according to the position instability of the balloon receiver. Therefore the accurate formula of bistatic balloon-borne radar sensitivity depends on nature RCS of stealth target and the position instability of the balloon receiver, it should be written as:

$$SNR_B(r, \phi, \theta) = M \frac{RCS_B(r, \phi, \theta)}{R_t^2 R_r^2}, \quad (33a)$$

$$M = \frac{P_t G_t G_r \lambda^2}{(4\pi)^3 K T_s B_n L}. \quad (33b)$$

From (33) and (31), the accurate form of random range and angular measurement error SNR depend on RCS of stealth target predicted by (PO) method in Section 3 and are given by

$$\sigma_{RN} = \frac{C}{8B \sqrt{\frac{M \cdot RCS_B(r, \phi, \theta)}{R_t^2 R_r^2}}}, \quad (34a)$$

$$\sigma_{\phi N} = \sigma_{\theta N} = \frac{\theta_B / \cos(\phi \text{ or } \theta)}{K_M \sqrt{2 \left(\frac{M \cdot RCS_B(r, \phi, \theta)}{R_t^2 R_r^2} \right)}}. \quad (34b)$$

By using the differential (29) and it can be expressed in the matrix form [22]:

$$\begin{bmatrix} dr \\ d\phi \\ d\theta \end{bmatrix} = \begin{bmatrix} C_{R1} + C_{T1} & C_{R2} + C_{T2} & C_{R3} + C_{T3} \\ -\frac{\sin^2 \phi}{y - y_R} & \frac{\cos^2 \phi}{x - x_R} & 0 \\ \frac{C_{R3} \cos \phi}{r_R} & -\frac{C_{R3} \sin \phi}{r_R} & \frac{\cos \theta}{r_R} \end{bmatrix} \begin{bmatrix} dx \\ dy \\ dz \end{bmatrix} + \begin{bmatrix} k_r \\ k_\phi \\ k_\theta \end{bmatrix} \quad (35a)$$

where

$$C_{i1} = \frac{x - x_i}{r_i}, C_{i2} = \frac{y - y_i}{r_i}, C_{i3} = \frac{z - z_i}{r_i}, \quad i = (R, T), \quad (35b)$$

$$k_r = -[C_{R1} dx_R + C_{R2} dy_R + C_{R3} dz_R], \quad (35c)$$

$$k_\phi = \frac{\sin^2 \phi}{y - y_R} dx_R - \frac{\cos^2 \phi}{x - x_R} dy_R, \quad (35d)$$

$$k_\theta = \frac{C_{R3} \cos \phi}{r_R} dx_R + \frac{C_{R3} \sin \phi}{r_R} dy_R + \frac{\cos \theta}{r_R} dz_R, \quad (35e)$$

or

$$dV = \mathbb{C}dX + dS \quad (36)$$

where \mathbb{C} (3×3) is the matrix of coefficients, dX (3×1) is the vector of stealth target's position error, dV (3×1) is the vector measurement of stealth target's position and dS (3×1) is the vector pertaining to all random measurement error according to position instability of balloon receiver. The solution of (36) is

$$dX = \mathbb{C}^{-1}(dV - dS). \quad (37)$$

The corresponding covariance matrix of the stealthy target position error is [22]:

$$P_{dX} = \mathbb{C}^{-1}\{E[dVdV^T] + E[dSdS^T]\}\mathbb{C}^{-T}. \quad (38)$$

The expressions of $E[dVdV^T]$ and $E[dSdS^T]$ are given by

$$E[dVdV^T] = \text{diag}[\sigma_r^2 \quad \sigma_\phi^2 \quad \sigma_\theta^2], \quad (39a)$$

$$E[dSdS^T] =$$

$$\begin{bmatrix} 2 & 0 & 0 \\ 0 & \frac{1}{r_R^2 \cos^2 \theta} & \frac{(\sin \phi - \cos \phi) \sin^2 \phi \sin \theta}{2r_R} \\ 0 & \frac{(\sin \phi - \cos \phi) \sin 2\phi \sin \theta}{2r_R} & \frac{1}{r_R^2} \end{bmatrix} \begin{bmatrix} \sigma_{x_R}^2 \\ \sigma_{y_R}^2 \\ \sigma_{z_R}^2 \end{bmatrix} \quad (39b)$$

where $\sigma_{x_R}, \sigma_{y_R}, \sigma_{z_R}$ are the position instability measurement errors of the balloon receiver

The RMSE is used to describe the stealthy target position accuracy, from (38), (39a) and (39b), it is noted that the stealthy position accuracy is related to the position of the considered target and the deployment of the two sites in the bistatic system. So it is called GDOP (Geometrical Dilution Of Position). The expression of the GDOP is [23]:

$$GDOP = \sqrt{\text{tr}[P_{dX}]}. \quad (40)$$

The radar and target parameters are illustrated in Tab. 1.

Parameter	Value
P_t (kWatt)	250
G_t, G_r (dB)	32
f (MHz)	3000
B_n (MHz)	1
L_t, L_r (dB)	5
σ_{RF} (m)	3
σ_{RB} (m)	10
ΔR (m)	10
$\sigma_{\phi F}$ (mrad)	0.2
$\sigma_{\theta F}$ (mrad)	0.2
$\sigma_{\phi B}$ (mrad)	0.5
$\sigma_{\theta B}$ (mrad)	0.5
V (m/s)	400

Tab. 1. The radar and stealthy target parameters.

5. Simulation Results

5.1 Instability of Balloon-borne Receiver according to Wind Speed Results

For all problems considered, the ideal balloon position is fixed at ($X = 150$ km, $Y = 100$ km, $Z = 21$ km) from the ground-based transmitter. The balloon is initialized by flying at 1 m/s airspeed. With solving the optimal control problems, we neglect the contribution from centripetal acceleration, assuming acceleration is constant in the ENU farm, with a magnitude of 0.029 m/s^2 . The simulation displays the positional instability of the balloon-borne receiver according to the horizontal wind speed, taking 250 seconds of random wind as an example, σ_w is of 15 m/s shown in Fig. 6. It is clear that the mean wind velocity at altitude of 21 km varies randomly between -15 to +15 m/s. Fig. 7 shows the comparison between the ideal position and unstable balloon position in X-direction and Y-direction. It is clear that the balloon suspends in the stratosphere about 21 km above the Earth and extends in a sphere of 0.5 km radius.

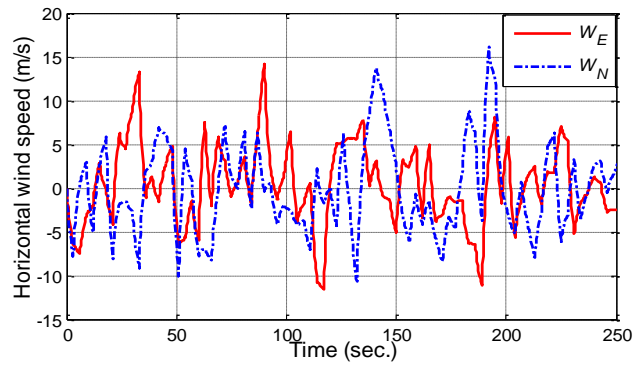
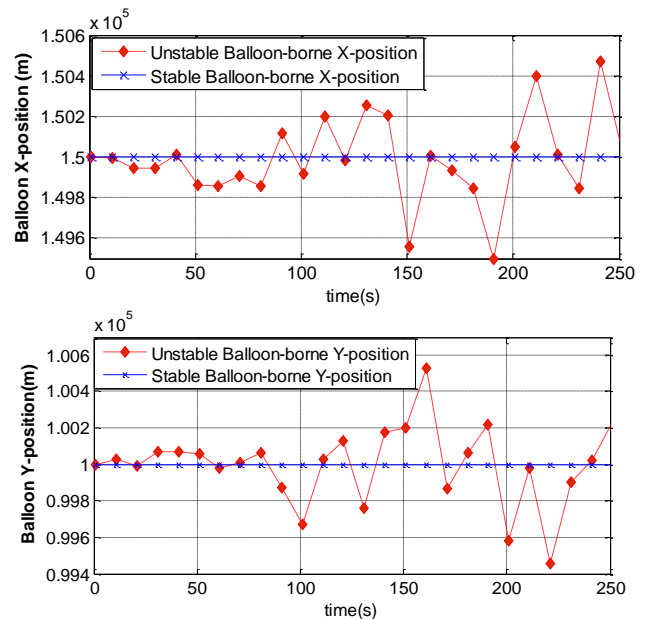


Fig. 6. Simulation of random horizontal wind speed.



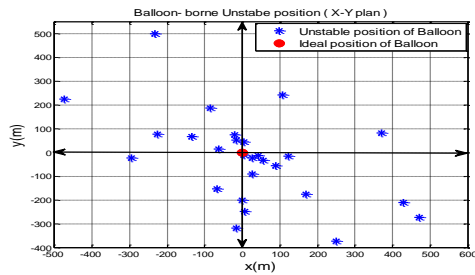


Fig. 7. The comparison between the ideal position and unstable balloon position in X-direction and Y-direction.

5.2 Establishing the Stealthy Target Model and Stealthy RCS Results

Fig. 8(a) shows the geometry model and scatters of stealth target F-117A in the range of $(0 \leq \theta \leq 360)$ and $(0 \leq \phi \leq 360)$. Fig. 8(b) shows 3-D RCS of the stealth target in bistatic system. A comparison of 2-D bistatic RCS within different aspect angle θ according to the altitude of bistatic receiver is demonstrated in Fig. 9(a). We further assume that the incident wave is (θ -polarized), frequency is 3 GHz and elevation angle takes two values ($\theta = 80$ and 120 degree) while azimuth angle ϕ between the horizon and observation direction varies from $(0$ to 360 degrees). It is clear that the RCS with a higher aspect angle in balloon-borne radar is better than with lower aspect angles in ground-based bistatic system. Fig. 9(b) shows the results in 2-D polar plot.

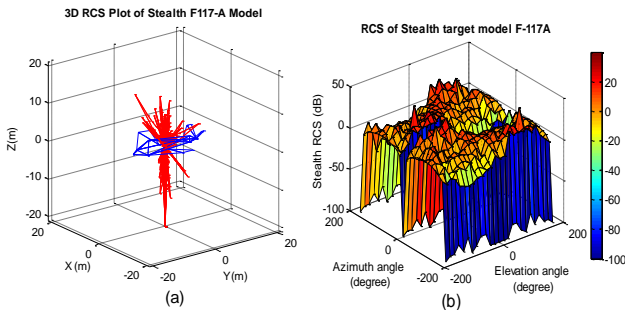


Fig. 8. Bistatic RCS of the stealthy target based on F-117A in 3-D.

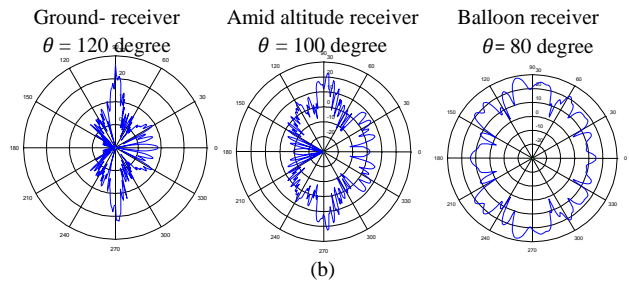
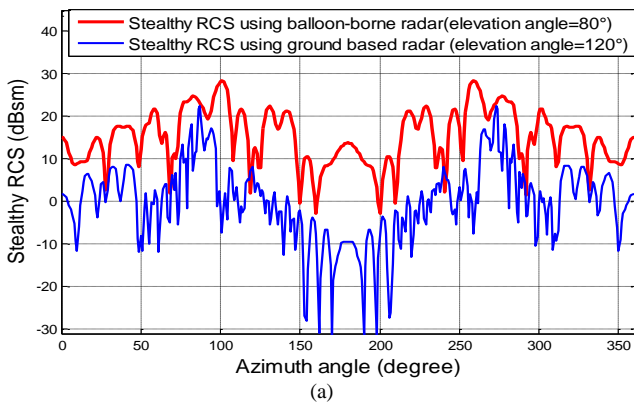


Fig. 9. a) Comparison of RCS within different aspect angle θ according to the altitude of bistatic receiver in 2-D, b) the polar plot using different aspect angles.

5.3 SNR Results for Proposed Scheme under Balloon Positional Instability & Stealthy RCS

A comparison of radar sensitivity between the proposed scheme in balloon-borne radar and conventional ground-based bistatic system at X-direction is demonstrated in Fig. 10. To clearly indicate SNR fluctuation of real stealth target RCS in (X-axis) range, we assume that the stealth target is moving at constant altitude 17 km and constant velocity $V = 400$ m/s. Thus, as long as the range changes, the elevation aspect angle changes similarly, say the elevation angle $\theta_s = 180^\circ$ for ground-based radar while for balloon-borne radar $\theta_s = 0^\circ$, so as to satisfy the minimum range between radar and stealth target. The maximum range exists in the far field saturation, as elevation angle $\theta_s \approx 90^\circ$ for ground-based radar and $\theta_s \approx 50^\circ$ for balloon-borne radar. Fig. 10 is a comparison between the SNR of real stealth RCS subject to stable and unstable position of the balloon-borne and flat RCS (0.025 m^2) of conventional ground-based system. It is clear that the sensitivity of the proposed radar scheme has been improved due to increasing scatterer RCS of stealth model with a higher aspect angle comparing to the conventional system. The 3-D bistatic radar sensitivities of taking flat RCS (0.025 m^2) and stealth RCS are shown in Fig. 11.

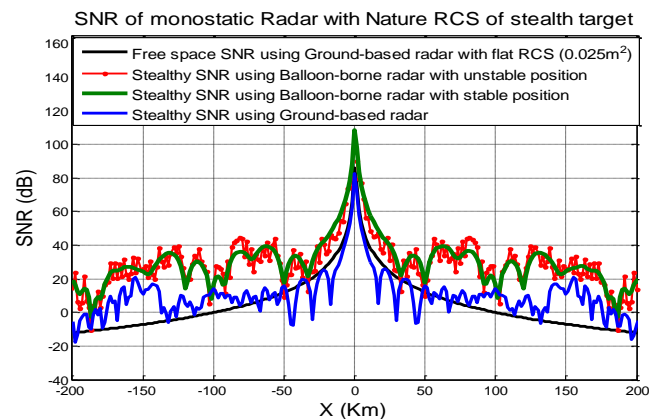


Fig. 10. A comparison between SNR for radar with real RCS of a stealth target under stable and unstable balloon position and ground-based system in X-direction.

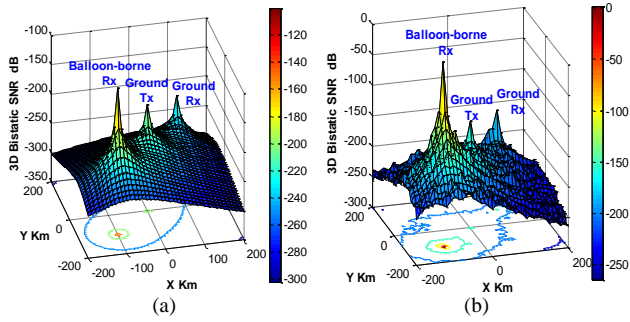


Fig. 11. 3D Bistatic radar sensitivity using (a) flat RCS (0.025 m²) and (b) real stealth RCS.

5.4 Simulation of Tracking a Stealthy Target

Fig. 12 shows RMSE in range and angle of stealthy target detection. It shows that RMSE of the proposed scheme under instable position has been improved comparing to the conventional ground-based radar by increasing scatterer RCS of stealth model with higher aspect angle. We can find that fluctuation of RMSE value under two cases shows a tendency around the flat (RCS = 0.025 m²) value along X-axis. From the RMSE plots, it shows that the

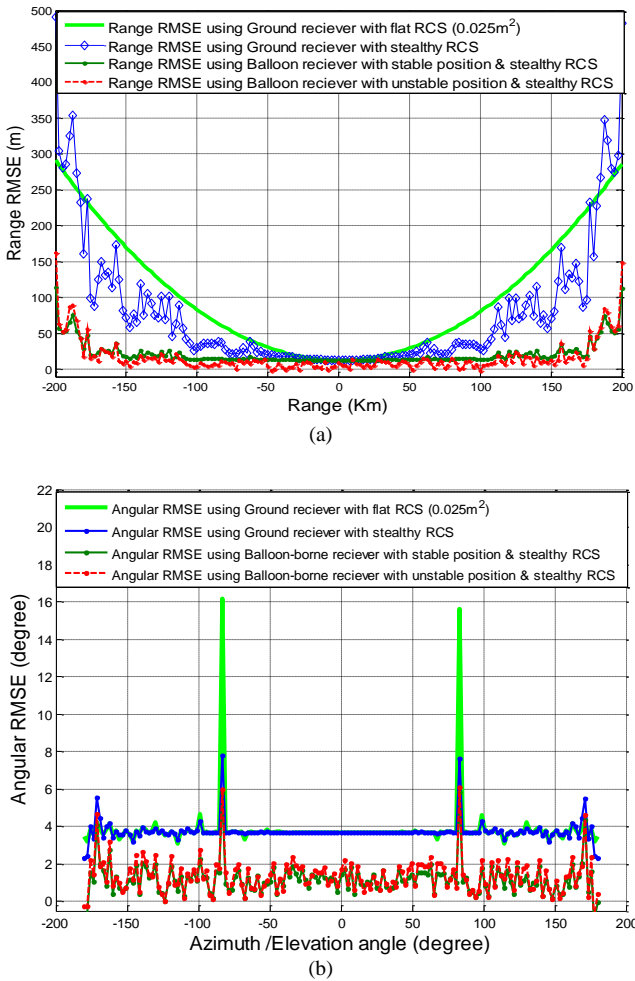


Fig. 12. A comparison between the (RMSE) of stealthy target detection with the proposed scheme and the conventional system.

value is increasing with range enlarging when ground-based system is applied. In balloon-borne system with instable position, RMSE becomes even less due to obtaining real stealth RCS. In ground-based system, nulls (less than 0 dB) of SNR increase along range axis up to the maximum range (200 km), while range RMSE reaches to 300 m, angle RMSE reaches to 4°. In cases of balloon-borne system under instable position, RMSE has been improved with less nulls existing, for the same maximum range, RMSE equals to 50 m, angular RMSE fluctuate around 1°.

Fig. 13 presents the contour plots of GDOP values for real stealth RCS data predicted by PO method in different radar geometrical structures. The instable balloon-borne platform is simulated under random wind by using Dryden turbulence model within an area of 400 km × 400 km. The stealth target flies at 17 km altitude. The ground-based transmitter (Tx) is located at (-150,150) km, ground-based receiver (Rx) is located at (150,150) km and the balloon-borne receiver (Rx) is located above (150,-150) km. The altitude of balloon-borne receiver is equal to 21 km. The GDOP of balloon-borne radar has been improved on conventional ground-based radar by higher aspect vision. The worst case is that the transmitter and the receiver both are ground-based. In this case, GDOP around ground-based receiver is poor that the inner contour (30 m) is located at 35 km and the outer contour (180 m) is located at 100 km. The optimal case is that the receiver is put on balloon-borne, it indicates that the GDOP results have been improved and accurately estimated due to decreasing RMSE of the stealth target detection, it is shown that the inner contour (30 m) is located at 150 km and the outer contour (180 m) is located at 350 km from the balloon-borne receiver. The results of Fig. 13 are summarized in Tab. 2.

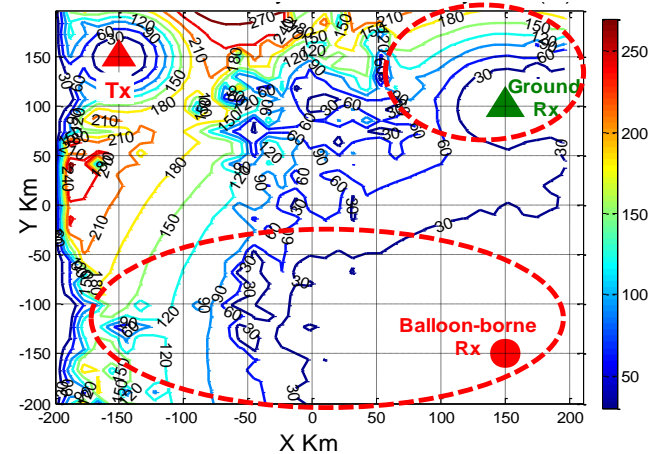


Fig. 13. The GDOP (m) comparison of balloon-borne and conventional ground-based bistatic system.

Radar type	GDOP of receiver (m)			
	Inner contour		Outer contour	
	Value	Range (km)	Value	Range (km)
Ground-based	30	35	180	100
Balloon-borne	30	150	180	350

Tab. 2. The GDOP of different geometrical structures.

It is found that GDOP of the proposed scheme has been improved due to decreasing the range and angular RMSE by increasing scatterer RCS of the stealth model comparing to the conventional ground-based system

In Fig. 14(a), the comparison between tracking of stealth target using the proposed scheme under instable position due to random wind speed and the conventional ground system. It is clear that the position estimate error of stealth target model was reduced by using the proposed scheme at all time interval due to increasing stealth RCS with a higher aspect vision as shown in Fig. 14(b).

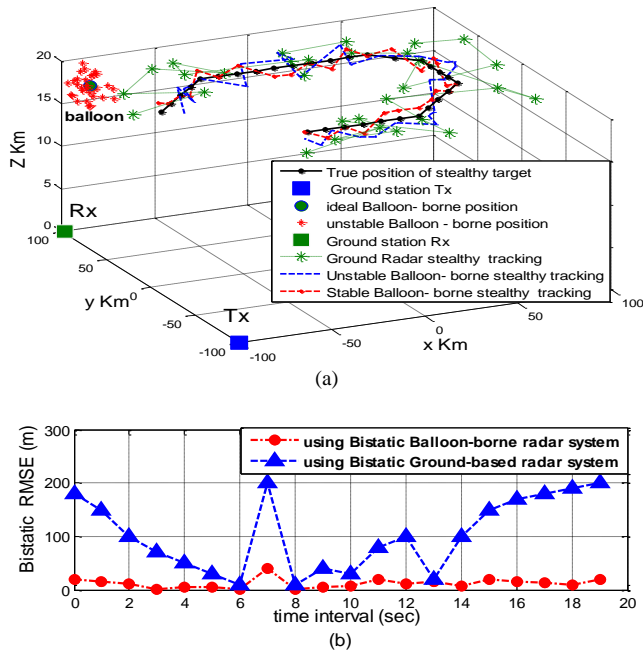


Fig. 14. The comparison between the tracking of stealthy target using balloon-borne bistatic system and conventional ground-based bistatic system.

6. Conclusion

An improvement of stealth RCS detection with higher aspect vision is presented. The stratospheric balloon positional instability due to random wind is considered. The results revealed that the proposed scheme demonstrates higher location accuracy than the conventional ground-based system. It is clear that bistatic radar sensitivity of the proposed scheme has been improved due to increasing scatterer RCS of stealth model with a higher aspect angle as predicted by PO method. The comparison between tracking of stealth target using the proposed scheme and the conventional system is introduced. The GDOP of the proposed scheme has been improved due to decreasing RMSE of the balloon radar system comparing to the conventional system. Finally the proposed system has better performance at almost all time intervals.

Acknowledgments

This work is supported by the China National Found of “863 Project”, Ref. 2013AA7010051.

References

- [1] CHEN, X., GUAN, J., LIU, N., HE, Y. Maneuvering target detection via Radon-Fractional Fourier transform-based long time coherent integration. *IEEE Trans. Signal Process.*, 2014, vol. 62, no. 4, p. 939–953.
- [2] TENG, Y., GRIFFITHS, H.D., BAKER, C.J., WOODBRIDGE, K. Netted radar sensitivity and ambiguity. *IET Radar Sonar Navig.*, December 2007, vol. 1, no. 6, p. 479–486.
- [3] KUSCHEL, H., HECKENBACH, J., MULIER, ST., APPEL, R. Countering stealth with passive, multi-static, low frequency radars. *IEEE Aerospace and Electronic Systems Magazine*, 2010, vol.25, no. 9, p. 11–17.
- [4] KUSCHEL, H., HECKENBACH, J., MULIER, ST., APPEL, R. On the potentials of passive, multistatic, low frequency radars to counter stealth and detect low flying targets. In *IEEE Conference, RADAR '08*, 2008, p. 1–6.
- [5] HOWE, D. Introduction to the basic technology of stealthy aircraft: Part 2- Illumination by the enemy (active considerations). *Journal of Engineering for Gas Turbines and Power*, 1991, vol. 113, no. 1, p. 80–86.
- [6] EL-KAMCHOUCY, H., SAADA, K., HAFEZ, A. Optimum stealthy aircraft detection using a multistatic radar. *ICACT Transactions on Advanced Communications Technology (ICACT-TACT)*, 2013, vol. 6, no. 2, p. 337–342.
- [7] DENG, H. Orthogonal netted radar systems. *IEEE Aerospace and Electronic Systems Magazine*, 2012, vol. 27, no. 5, p. 28–35.
- [8] BEZOUSEK, P., SCHEJBAL, V. Bistatic and multistatic radar systems. *Radioengineering*, 2008, vol. 17, no. 3, p. 53–59.
- [9] AXIOTIS, D. I., THEOLOGOU, M. E., SYKAS, E. D. The effect of platform instability on the system level performance of HAPS UMTS. *IEEE Communications Letters*, 2004, vol. 8, no. 2, p. 111 to 113.
- [10] BEAL, T. R. Digital simulation of atmospheric turbulence for Dryden and von Karman models. *Journal of Guidance, Control, and Dynamics*, 1993, vol. 16, no. 1, p. 132–138.
- [11] FORTUNATI, S., FARINA, A., GINI, F., GRAZIANO, A., GRECO, M. S., GIOMPAPA, S. Impact of flight disturbances on airborne radar tracking. *IEEE Transactions on Aerospace and Electronic Systems*, 2012, vol. 48, no. 3, p. 2698 –2710.
- [12] HOGGE, E. B-737 linear autoland simulink model. NASA, *Technical Report NASA/CR-2004-213021*, 2004.
- [13] MIELE, A., WANG, T., MELVIN, W. W. Optimal take-off trajectories in the presence of wind shear. *Journal of Optimization Theory and Applications*, 1986, vol. 49, no. 1, p. 1–45.
- [14] FELDMAN, M. A. Efficient low-speed flight in a wind field. *Master Thesis*. Blacksburg, VA, Virginia Polytechnic Inst. and State Univ., July 1996.
- [15] LEE, S., BANG, H. Three-dimensional ascent trajectory optimization for stratospheric airship platforms in the jet stream. *Journal of Guidance, Control, and Dynamics*, 2007, vol. 30, no. 5, p. 1341 to 1352.

- [16] UPENDRA, A., BALAKRISHNAN, J. A novel method for RCS reduction of a complex shaped aircraft using partial RAM coating. *International Journal of Engineering and Innovative Technology (IJEIT)*, 2012, vol. 2, no. 2, p. 52–56.
- [17] LI, J., WANG, X., QU, L. Calculation of physical optics integrals over NURBS surface using a delaminating quadrature method. *IEEE Transactions on Antennas and Propagation*, 2012, vol. 60, no. 5, p. 2388–2397.
- [18] MOREIRA, F. J. S., PRATA, A. JR. A self-checking predictor-corrector algorithm for efficient evaluation of reflector antenna radiation integrals. *IEEE Transactions on Antennas and Propagation*, 1994, vol. 42, no. 2, p. 246–254.
- [19] CORUCCI, L., GIUSTI, E., MARTORELLA, M., BERIZZI, F. Near field physical optics modelling for concealed weapon detection. *IEEE Transactions on Antennas and Propagation*, 2012, vol. 60, no. 12, p. 6052–6057.
- [20] CORBEL, C., BOURLIER, C., PINEL, N., CHAUVEAU, J. Rough surface RCS measurements and simulations using the physical optics approximation. *IEEE Transactions on Antennas and Propagation*, 2013, vol. 61, no. 10, p. 5155–5165.
- [21] CURRY, G. R. *Radar System Performance Modeling*. Second Edition, 2005.
- [22] WEI, W., HE, L. The location method and accuracy analysis for bistatic systems. In *National Aerospace and Electronics Conference (NAECON)*. Dayton (OH, USA), 1994, p. 62–65.
- [23] ZHAO KONGRUI, YU CHANGJUN, ZHOU GONGJIAN, QUAN TAIFAN. Altitude and RCS estimation with echo amplitude in bistatic high frequency surface wave radar. In *16th*

International Conference on Information Fusion. Istanbul (Turkey), 2013, p. 1342–1347.

About Authors ...

Mohamed A. BARBARY received the B.Sc degree in Electronics and Communications in 2003 and the M.Sc. in Electrical Engineering in 2012, both from the Faculty of Engineering, Alexandria University, Egypt. He is currently working towards the Ph.D. degree in the College of Electronic and Information Engineering, Nanjing University of Aeronautics and Astronautics (NUAA), Nanjing, China. He received many technical courses in radar, stealth target detection and electronic engineering design and implementation and worked as radar system engineer for more than 4 years.

Peng ZONG received the B.Sc. from Nanjing University of Aeronautics and Astronautics (NUAA), China, and Ph.D. degrees from University of Portsmouth, UK. He has been a professor in College of Astronautics NUAA since 2006. His academic experience is research fellow in the Centre for Communication Systems Research, University of Surrey, England in 2001, following by employee of Hughes Network System (USA) as software engineer and chief designer in Information and Technology Institute of China Aerospace Science & Industry Corp. (CASIC) until 2006. His research fields are mobile communication, satellite networking mostly concerned by routing algorithm of LEO constellation, and stealthy detection of netting radar.